crystals

MDPI

Article

Unveiling the Transporting Mechanism of $(Ti_{0.2}Zr_{0.2}Nb_{0.2}Hf_{0.2}Ta_{0.2})C$ at Room Temperature

Tao Liu [1,2], Liwen Lei [1], Jinyong Zhang [1,2,*] and Neng Li [1,3,*]

[1] State Key Laboratory of Advanced Technology for Materials Synthesis and Processing, Wuhan University of Technology, Wuhan 430070, China; lt164357@163.com
[2] Hubei Longzhong Laboratory, Xiangyang 441000, China
[3] Key Laboratory of Green Chemical Engineering Process of Ministry of Education, Novel Catalytic Materials of Hubei Engineering Research Center, School of Chemistry and Environmental Engineering, Wuhan Institute of Technology, Wuhan 430205, China
* Correspondence: jyzhang@whut.edu.cn (J.Z.); lineng@whut.edu.cn (N.L.)

Abstract: High-entropy materials have been widely researched in recent years, and more work on their thermal and electrical properties is still needed. Herein, we fabricate a high-entropy carbide $(Ti_{0.2}Zr_{0.2}Nb_{0.2}Hf_{0.2}Ta_{0.2})C$ ceramic and report the thermal and electrical conductivity at room temperature using first-principles calculations and experiments. The movement of phonons is suppressed in high-entropy carbides when analyzing the thermal and electrical conductivity at room temperature, but the movement of electrons is not. After the first-principles calculations on the electronic structure and lattice vibration and experiments, we give the reasons why the rule of mixture can predict electrical conductivity but not thermal conductivity at room temperature. Finally, we outline the cause of the similar lattice patterns between TaC and $(Ti_{0.2}Zr_{0.2}Nb_{0.2}Hf_{0.2}Ta_{0.2})C$.

Keywords: high-entropy carbides; thermal conductivity; electrical conductivity; density function theory

check for updates

Citation: Liu, T.; Lei, L.; Zhang, J.; Li, N. Unveiling the Transporting Mechanism of $(Ti_{0.2}Zr_{0.2}Nb_{0.2}Hf_{0.2}Ta_{0.2})C$ at Room Temperature. *Crystals* **2023**, *13*, 708. https://doi.org/10.3390/cryst13040708

Academic Editors: Zhijian Sun and Vladislav V. Kharton

Received: 25 February 2023
Revised: 14 April 2023
Accepted: 18 April 2023
Published: 21 April 2023

Copyright: © 2023 by the authors. Licensee MDPI, Basel, Switzerland. This article is an open access article distributed under the terms and conditions of the Creative Commons Attribution (CC BY) license (https://creativecommons.org/licenses/by/4.0/).

1. Introduction

High-entropy ceramics have attracted widespread attention due to their designability in terms of composition and related properties. Rost et al. [1] first reported and fabricated a high-entropy oxide in 2015; high-entropy ceramics contain oxides [2–5], borides [6–8], silicides [9–11], carbides [12–17], nitrides [18] and more at present. High-entropy carbides have a higher indentation modulus and hardness, attributed to the bonding behavior and solid solution hardening originating from localized lattice strains, than those calculated via the rule of mixture (ROM) from the individual binary carbides [12,16]. First-principles calculations are also used to study high-entropy ceramics. Beilin Ye et al. [19,20] theoretically demonstrated the formation possibility of $(Hf_{0.2}Zr_{0.2}Ta_{0.2}Nb_{0.2}Ti_{0.2})C$ and $(Zr_{0.25}Nb_{0.25}Ti_{0.25}V_{0.25})C$. Based on these, Shi-Yu Liu et al. [21] and Wenyu Lu et al. [22] gave the theoretical mechanical properties of these high-entropy carbides, providing ideas for the design of high-entropy materials.

The electrical and heat transport of high-entropy carbides constitute an important topic of study due to their extremely low thermal conductivity at room temperature. Evan C. Schwind et al. found that the room temperature thermal conductivity of $(TaHfNbZr)C_4$ is 10.7 W/m·K (97.6% relative density) [23], Yan et al. found that $(Hf_{0.2}Zr_{0.2}Ta_{0.2}Nb_{0.2}Ti_{0.2})C$ (93% relative density) has a thermal conductivity of 6.45 W/m·K [14] and Liu et al. reported that the room temperature thermal conductivity of (VNbTaMoW)C is 9.2 W/m·K (97.7% relative density) [17], all of which are much lower than the individual binary carbides (about 10~33.5 W/m·K). Some researchers believed that these high-entropy carbides exhibit a lower room temperature thermal conductivity compared to that calculated from the rule of mixtures because of the terrible lattice dislocation and point defects. D. Liu

et al. [24] stated that the difference in C content causes a change in bonding within the specimen: as the molar fraction of C changes from 0.35 (about 16 W/m·K) to 0.5 (about 9 W/m·K), the bonding transitions from metallic to covalent in ceramics, which leads to a significant decrease in thermal conductivity. F.-Z. Dai et al. [25] calculated lattice thermal conductivity via deep learning, which decreases with the increase in temperature. E.C. Schwind. et al. [23] showed the thermal conductivity with temperature changes and noted that for (Ti, Hf, Nb, Zr)C, electrical thermal conductivity plays a dominant role.

However, detailed work assessing the performance of electrons and phonons in high-entropy carbides, and showing the thermal conductivity is lower than the predicted value under the ROM, is still lacking. Additionally, research on what physical properties of high-entropy carbides can be predicted by the ROM and the reasons behind this is also lacking. Thus, in this work, we used the SPS process to synthesize and prepare dense $(Ti_{0.2}Zr_{0.2}Nb_{0.2}Hf_{0.2}Ta_{0.2})C$ (HEC), and than measured thermal and electrical conductivity and carried out first-principles calculations to supplement the related research on high-entropy carbides. Here, we conclude that, in high-entropy carbides, phonon transport is more severely affected than electron transport at room temperature because the high-entropy effect has a greater effect on the lattice vibration and weakens the ability of acoustic phonons for heat transport. Moreover, the lattice distortion caused by the high-entropy effect also exacerbates phonon scattering and impedes heat transfer. However, the electron-dominated electrical conductivity and electrical thermal conductivity is not seriously suppressed as the electronic structure is not significantly affected.

2. Experimental and Theoretical Methods

2.1. Materials Synthesized

The $(Ti_{0.2}Zr_{0.2}Nb_{0.2}Hf_{0.2}Ta_{0.2})C$ was self-synthesized using commercial metal powders of Ti (AR, purity 98 wt%), Nb (AR, purity 99.8 wt%), Ta (AR, purity 99.8 wt%), Zr (AR, purity 99.8 wt%), Hf (AR, purity 99.8 wt%) and carbon black (200 nm) with Ti, Nb, Ta, Zr and Hf at 10 mol% and carbon black at 50 mol%. All the powders were mixed using a planetary ball mill at 240 r/min for 12 h with WC balls and ethanol as milling media. The ball-to-powder ratio was 3:1 in weight. After drying in the vacuum drying oven and dispersed through a 200-mesh sieve, the powder mixtures were sintered through Spark Plasma Sintering (SPS) at 1900 °C with a pressure of 50 MPa for 10 min and a heating rate of 100 °C/min. More details can be found in our previous work [26].

2.2. Properties Characterization

The phase compositions of the specimens were determined via X-ray diffraction (XRD, Rigaku Ultima III) with Cu K_α radiation, at a range of 20–90° and a step size of 0.02°. Additionally, the microstructures of the specimens were observed using scanning electron microscopy (SEM, Hitachi 3400). Isobaric heat capacity (C_p, J/g·K) and thermal diffusivity (α, cm^2/s) were measured using Discovery Laser Flash (TA DLF-2800) and a high-temperature calorimeter (Setaram MHTC 96). Electrical conductivity (σ, s/m) was measured via Cryoall CTA-3. Additionally, the bulk density (ρ, g/cm^3) was measured via the Archimedes method. Thermal conductivity (κ, W/m·K) was calculated according to the following equation, Equation (1).

$$\kappa = \alpha \times C_p \times \rho \tag{1}$$

2.3. Density Function Theory Calculations

The thermal and electrical properties were calculated using the CASTEP [27,28] based on density function theory (DFT). The exchange correlation interactions were described via the generalized gradient approximation (GGA) with PBE functional [29], and the ultra-soft pseudopotential method was used to express the interactions between ionic core and valence; the Brillouin Zone was sampled with $3 \times 2 \times 3$ *k*-points and a cutoff energy of 320 eV. Additionally, the self-consistence convergence tolerance for the total energy was

1.0×10^{-5} eV/atom, the maximum force of the atom was 0.03 eV/Å, the maximum stress was 0.05 GPa and the maximum ionic displacement was 1.0×10^{-3} Å. The lattice of HEC here was taken to be the Face-Centered Cubic (FCC) type, the same as that of previous publications [17,30,31]. An FCC supercell with 108 atoms, including Ti, Nb, Zr, Ta, Hf and C, at an atomic ratio of 1:1:1:1:1:5, was created using the Atomsk. The metal cations were randomly distributed in the unit cell. Therefore, the lowest symmetry of the triclinic lattice was chosen in the following calculation.

3. Results and Discussion

3.1. Crystal Structure and Morphology Characteristic

The SEM photograph of the fracture surface of the HEC at different scales is characterized in Figure 1a,b. Apart from a few small pores in the grain boundary, the sample shows a high density. This is consistent with the measured relative density of about 95%. More information can be found in previous work [26]. Figure 1c presents the typical XRD pattern of the $(Ti_{0.2}Zr_{0.2}Nb_{0.2}Hf_{0.2}Ta_{0.2})C$ (HEC) sample at 1900 °C and theoretic TaC pattern as a reference. It was seen that the single phase of $(Ti_{0.2}Zr_{0.2}Nb_{0.2}Hf_{0.2}Ta_{0.2})C$ formed at 1900 °C. Furthermore, the XRD pattern of TaC (PDF#77-0205) is more similar to the as-received high-entropy carbide than other individual carbides. A high-entropy carbide ceramic $(Ti_{0.2}Zr_{0.2}Nb_{0.2}Hf_{0.2}Ta_{0.2})C$ with good density and a single phase was fabricated in this work. Figure 1d,e show a comparison of the XRD patterns before and after the structural optimization of the high-entropy carbide; the optimized structure is in line with HEC, which indicates that the model in our task is reasonable.

3.2. Thermal and Electrical Conductivity of HEC

Figure 2a gives the measured electrical conductivity and thermal conductivity of the received HEC at room temperature, Figure 2b gives the measured electrical and lattice thermal conductivity of the received HEC at room temperature, and those of the referenced individual carbides [32]. Compared with them, the electrical conductivity of HEC is lower than that of TaC, higher than those of HfC and ZrC, and close to those of TiC and NbC. Additionally, the electrical conductivity of the as-received HEC is about 1.45×10^6 Sm^{-1} at room temperature, which is a little higher than that predicted by the ROM (1.35×10^6 Sm^{-1}). From previous reports [23,33], the high-entropy effect has both advantages and disadvantages for electron transport. Therefore, the electrical conductivity of HEC is slightly higher than the calculated ROM one (~3.7% difference) and can be predicted with the ROM value at this condition. Different from the electrical conductivity, the thermal conductivity exhibits a larger difference (~24.8% difference) with the ROM, which means that the ROM may not be suitable for the prediction of thermal conductivity due to the fact that thermal conductivity is not only determined by the electric structure but also by the structure of the crystalline.

To determine the reason for the difference between the measured and predicted values, the contributions of electrons and phonons to thermal conductivity were calculated. The total thermal conductivity (κ_t) of ceramic is equal to the sum of electrical (κ_e) and lattice (κ_L) thermal conductivity:

$$\kappa_t = \kappa_e + \kappa_L \tag{2}$$

$$\kappa_e = L \times \sigma \times T \tag{3}$$

Here, κ_e was calculated using the Wiedemann–Franz law, σ is electrical conductivity and T is temperature. L usually takes the Sommerfeld value ($L = 2.44 \times 10^{-8}$ $W\Omega K^{-2}$). However, the value of L is not a constant due to the influence of internal phonon–electron interactions [34]; to rigorously evaluate the heat conduction in more depth, a sophisticated theoretical expression developed by Makinson [35] was employed:

$$L_{th} = \frac{\frac{R_0}{R_{e-ph}} + \left(\frac{T}{\theta_D}\right)^5 J_5\left(\frac{\theta_D}{T}\right)}{\frac{R_0}{R_{e-ph}} + \left(\frac{T}{\theta_D}\right)^5 J_5\left(\frac{\theta_D}{T}\right)\left[1 + \frac{3}{\pi^2}\left(\frac{k_F}{q_D}\right)^2\left(\frac{\theta_D}{T}\right)^2 - \frac{1}{2\pi^2}\frac{J_7\left(\frac{\theta_D}{T}\right)}{J_5\left(\frac{\theta_D}{T}\right)}\right]} L_0 \quad (4)$$

where k_F is the Fermi wave vector, θ_D is the Debye temperature, q_D is the Debye wave vector and $\frac{k_F}{q_D} = 2^{-\frac{1}{3}}$ is derived from free electron theory. $J_n\left(\frac{\theta_D}{T}\right)$ is related to Debye and defined as:

$$J_n\left(\frac{\theta_D}{T}\right) = \int_0^{\frac{\theta_D}{T}} \frac{x^n e^x}{(e^x - 1)^2} dx \quad (5)$$

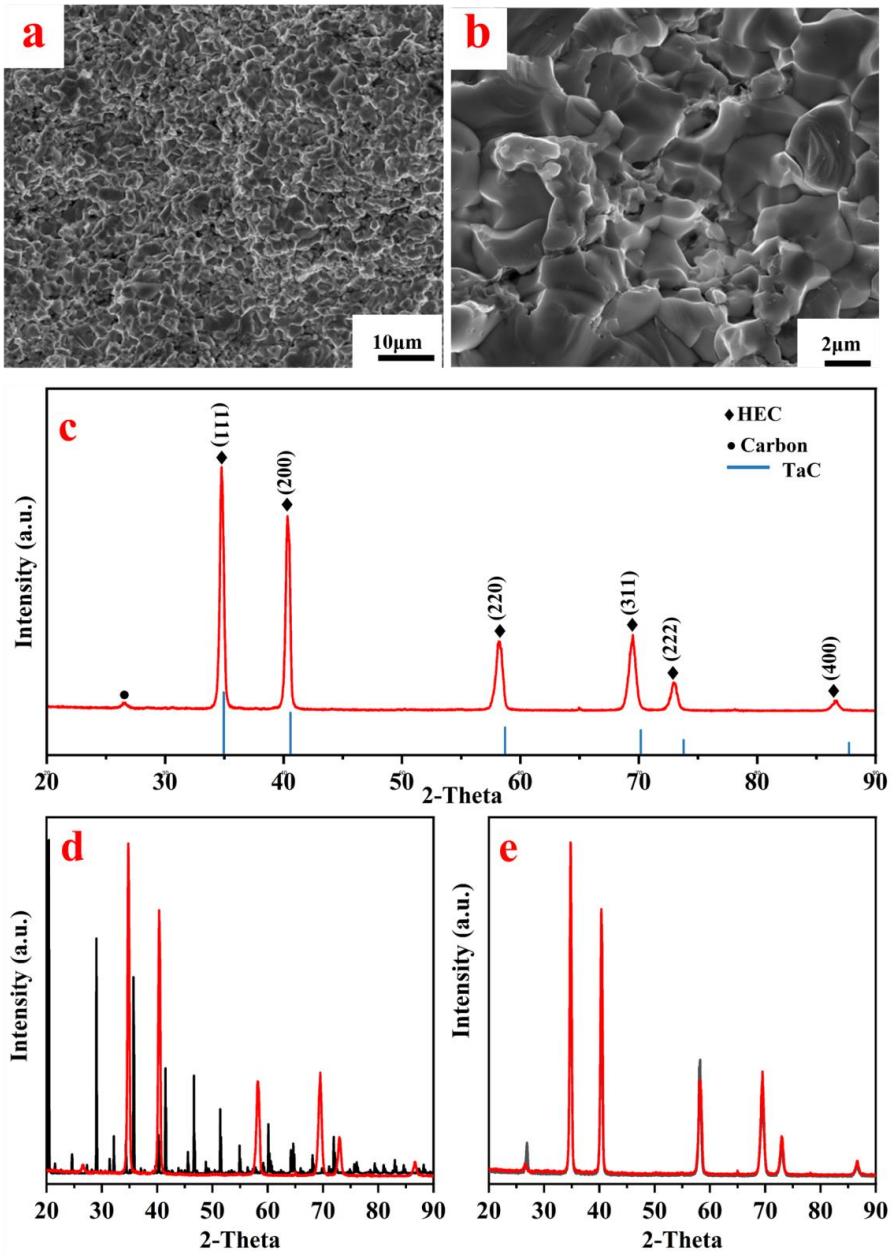

Figure 1. (**a**,**b**) SEM image of the HEC at different scales; (**c**) XRD patterns of the HEC and TaC; comparison of the experimental (red) and calculated (black) XRD patterns of the high−entropy car−bide; (**d**) before geometry optimization; (**e**) after geometry optimization.

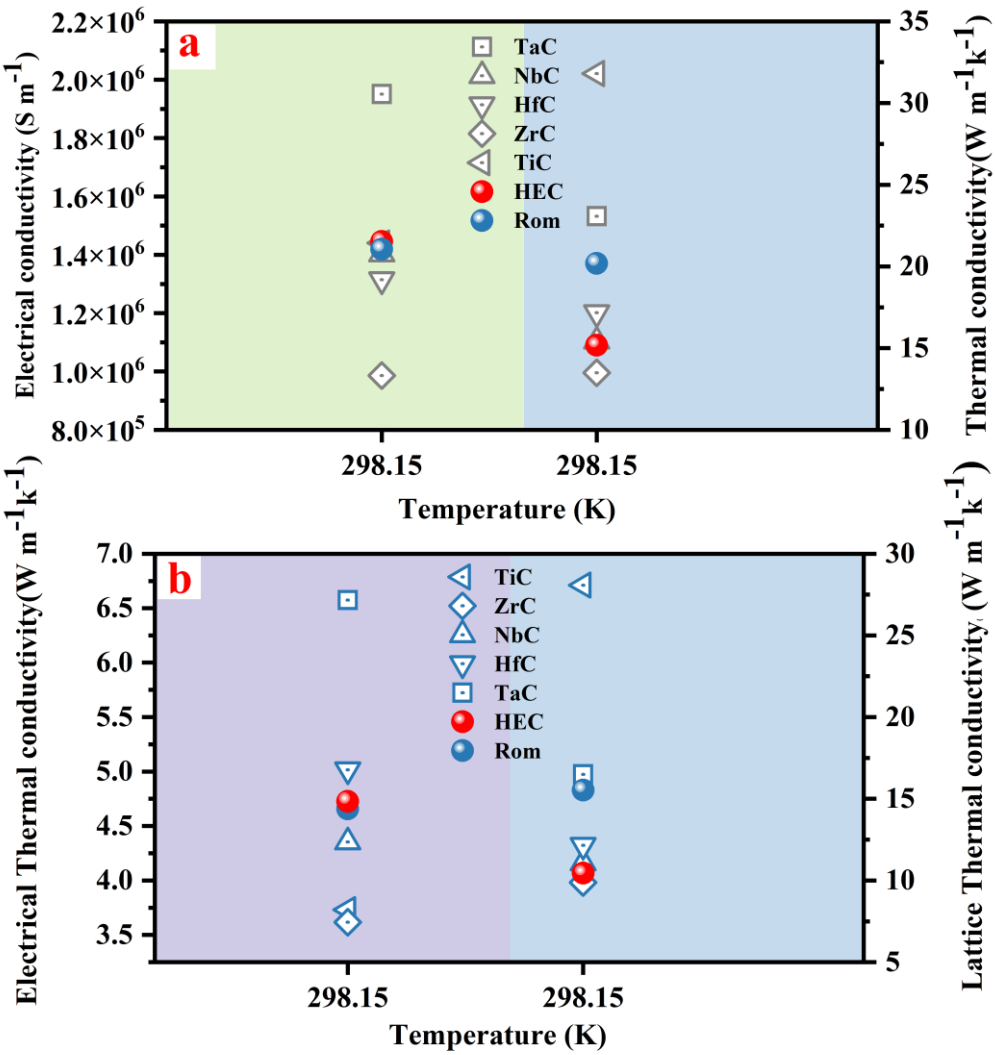

Figure 2. (**a**) Measured electrical and thermal conductivity of $(Ti_{0.2}Zr_{0.2}Nb_{0.2}Hf_{0.2}Ta_{0.2})C$ (sintered at 1900 °C) and binary carbides (TiC, ZrC, NbC, HfC and TaC) referenced from Xin Liang's report [32]; (**b**) the electrical thermal conductivity and lattice thermal conductivity for HEC and individual car−bides.

R_0, reflecting the extent of intrinsic disorder scattering, is the residual resistance at zero temperature: $R_{e\text{-}ph}$ is the electron–phonon scattering. Usually, we consider $\frac{R_0}{R_{e-ph}}$ and $\frac{\rho_0}{\rho_{e-ph}}$ to be numerically equal. ρ_0, residual electrical resistivity, can be approximately given by the relationship between ρ and T. Although $\rho_{e\text{-}ph}$ is commonly unknown due to the lack of electron–phonon scattering, in this work, since ρ exhibits excellent linear dependence with T, a good approximation can be measured: $R_{e-ph} = \frac{AT}{4\theta_D}$ and $\frac{A}{4\theta_D} = \frac{d\rho}{dT}$ [36,37]. Consequently, we obtain $\frac{d\rho}{dT}$, ρ_0 and θ_D [32,34] for HEC.

Figure 2b illustrates the contribution of electrons and phonons to the thermal conductivity of the HEC and individual carbides. As the transport of electrons is not seriously affected in HEC, the measured electrical thermal conductivity is similar to the predicated value of the ROM. However, the lattice thermal conductivity is not. Clearly, the phonon transport is significantly inhibited for HEC, so the lattice thermal conductivity is significantly lower than the predicted value, which caused the larger error between them.

3.3. Phonon Properties of HEC and Individual Carbides

As shown in Figure 3, the total density of phonon states (TPDOS) and partial density of phonon states (PPDOS) were calculated to assess the contribution of phonons to the lattice thermal conductivity One can distinctly see that both compounds have no imaginary frequencies as shown in Figure S1 (see Supplementary Information), proving that all of them are dynamically stable, and that phonon band gaps mainly originated from the large mass differences. Furthermore, Figure 3b gives the PPDOS of C atoms in HEC and individual carbides, showing a distinct vibration broadening of C. The vibration of Ti in HEC is lower than in TiC, but the gap of TiC is larger than HEC, as shown in Figure 3a,c. In general, a phonon broadening was observed in HEC, which is induced by the inherently present mass and force constant, unlike the individual carbides [38,39]. In low-frequency regions, the vibrations of different metal atoms increase the anharmonic interactions between phonons, hindering the thermal transport of low-frequency phonons and resulting in the decrease in lattice thermal conductivity [39]. Due to the high-entropy effect, the optical branching modes are more than individual carbides and move towards the low-frequency regions. These low-frequency optical branching modes result in a significant suppression of the frequency of the acoustic branch phonons, as shown in Figure S1 (see Supplementary Information), according to the "avoided crossing" effect [40]. The suppressed acoustic branch phonon comes from the contribution of heat transfer.

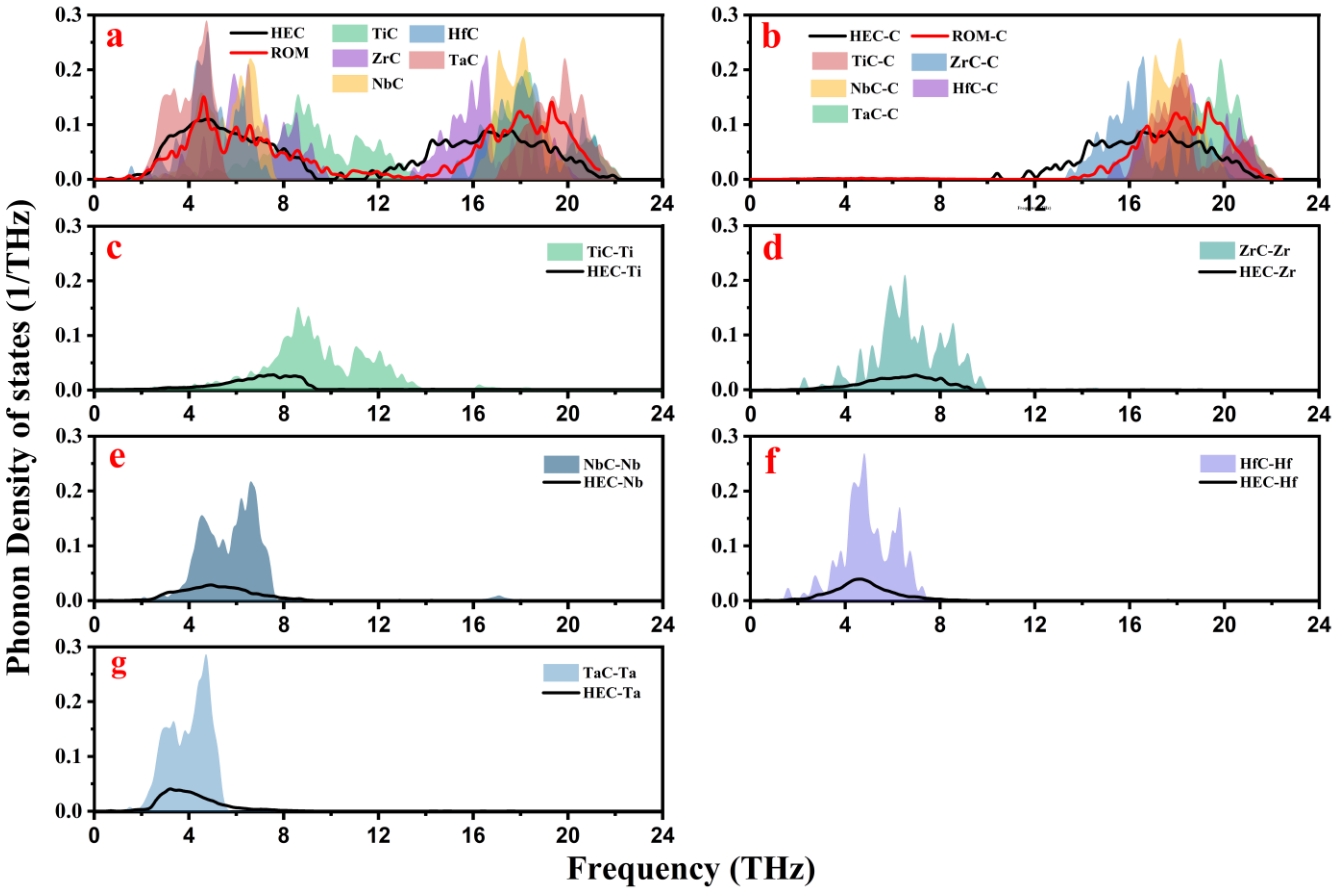

Figure 3. (**a**) Total phonon density of states of $(Ti_{0.2}Zr_{0.2}Nb_{0.2}Hf_{0.2}Ta_{0.2})C$ and individual carbides (TiC, NbC, ZrC, TaC, HfC); (**b**) the partial phonon density of states of C atom in HEC and individual carbides; (**c**–**g**) the partial phonon density of states of metal atom in HEC and individual carbides.

3.4. Electric Structure of HEC and Individual Carbides

To understand the bonding characteristics of HEC, the total density of state (TDOS) and partial density of state (PDOS) are shown in Figure 4. The Fermi level is situated near

a deep valley, which indicates the structural stability of high-entropy carbide [41]. Figure S2 presents the comparison between individual carbides and HEC; the Fermi levels of TiC and ZrC are much closer to the pseudogap bottom, whereas those of NbC, HfC and TaC deviate slightly from the pseudogap bottom. These characteristics imply that the stability of HEC is higher than that of NbC, HfC and TaC, but less than TiC and ZrC; a similar result to the reported report that has been found in previous work [42]. Below the Fermi level, the *M-d* orbitals are hybridized with *C-p* orbitals, which indicates strong covalent bonding between M and C atoms in HEC (see Supplementary Information). Uporov, S.A. et al. [43] pointed out that the values at Fermi level (V(EF)) are related with the electrical conductivity. Thereby, we obtained the V(EF) of HEC and ROM from Figure 4a, respectively. Distinctly, there was a small distance between them. According to Figure 4a, the TDOS of HEC is similar to the individual carbides, with no distinct difference among these compounds. As the metal atoms share a set of anionic sublattices in HEC, the PODS of metal atoms is lower than that of individual carbides, which is shown in Figure 4c–g. The "high entropy" results in a small change in the electronic structure from the analysis of TDOS and TPDOS.

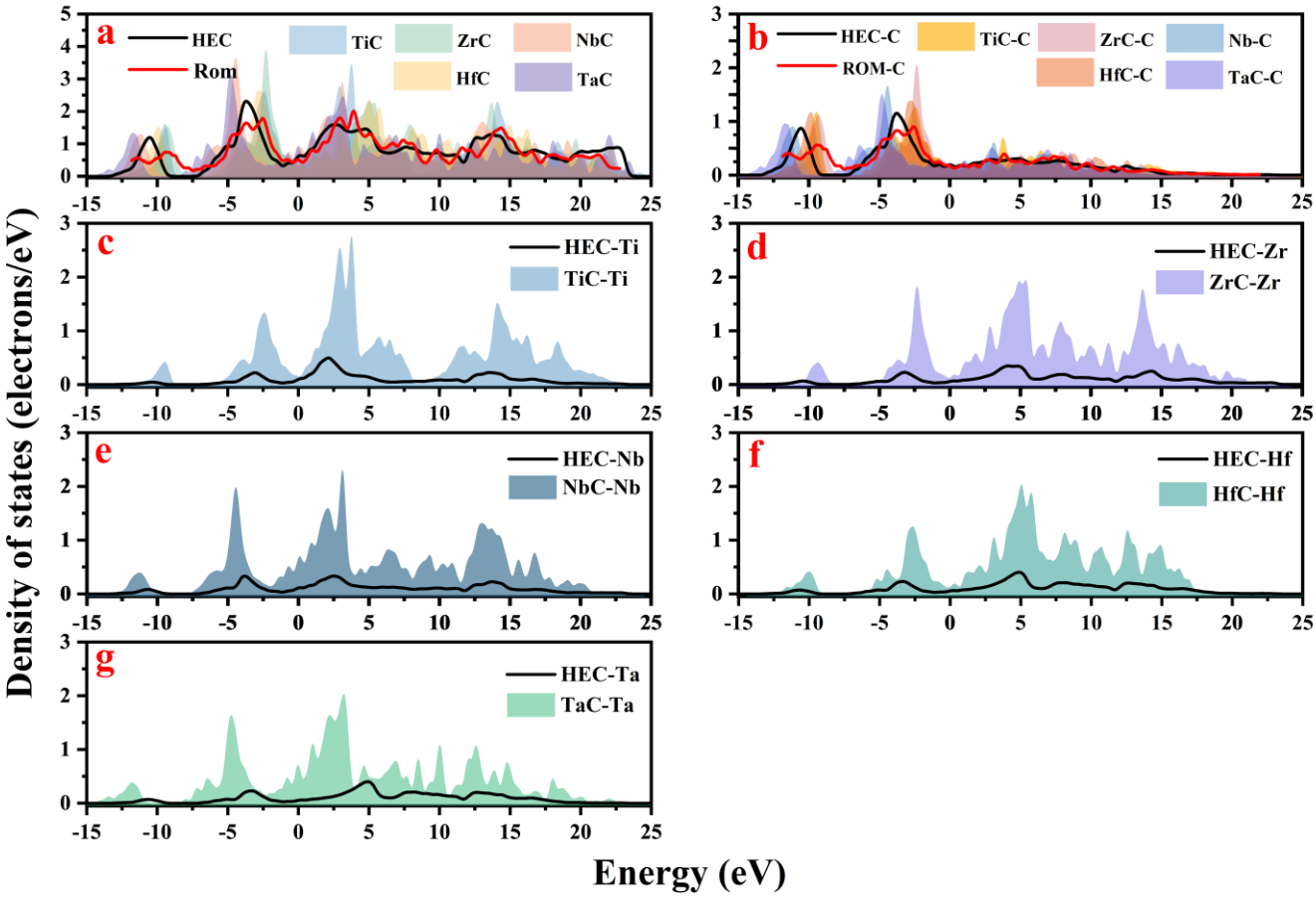

Figure 4. (**a**) Total−DOS of $(Ti_{0.2}Zr_{0.2}Nb_{0.2}Hf_{0.2}Ta_{0.2})C$ and individual carbides (TiC, NbC, ZrC, TaC, and HfC); (**b**) the partial−DOS of C atoms in HEC and individual carbides; (**c**−**g**) partial−DOS of metal atoms in HEC and individual carbides.

The Mulliken atomic populations (MAPs) of HEC and individual carbides are posted in Figure 5a,b. In the MAP, the positive/negative values represent that the element offers/accepts electrons [44]. Clearly, the metal atoms offer electrons and the C is the electrons' acceptor in HEC, and the transfer of charge also indicates the presence of an ionic characteristic in the bond attributed to the randomly distributed metal atoms, which induces the inhomogeneity of their local environment and the MAP of HEC is disordered, which is different with individual carbides. Ti, Zr and Nb atoms have higher levels of electron

transfer in HEC than individual carbides, Ta and Hf atoms are less so and C has a larger distribution, which is employed to compensate for cation charge disorder [45].

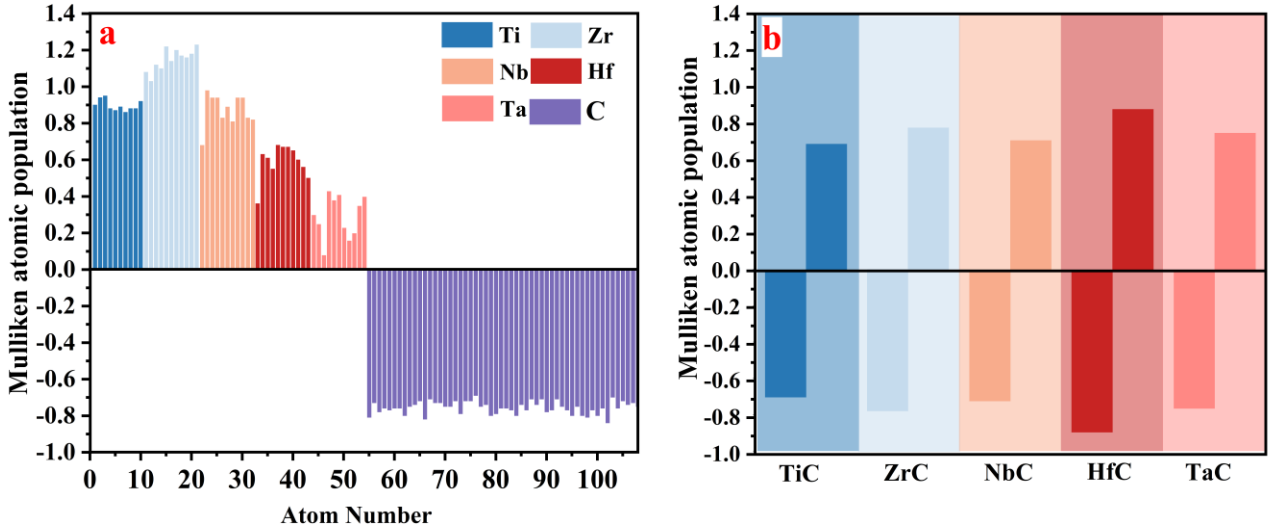

Figure 5. The Mulliken atomic population distribution for (**a**) HEC and (**b**) an individual carbide.

Concerning the transport of electrons and phonons in HEC, the reason why the transport of electrons is weakly affected is that the electronic structure of HEC changes lightly compared to individual carbides. For phonon transport, due to the suppression of acoustic phonons and phonon scattering, caused by lattice distortion, the heat transfer of phonons is reduced, thereby reducing the thermal conductivity of HEC.

3.5. Bond Characters

In Figure 6a, the BP-BL for M-C bonds is displayed depending on the DFT; it can be seen that, although the data are somewhat dispersed, the general trend is that a longer BL leads to a lower BP. Moreover, Marco Esters et al. [45] show that homogeneous coordination environments around the metals increase the configurational entropy, so that the bond lengths of different types of bonds are close to each other even though the distribution of bond lengths is disordered. Based on the XRD patterns, the $(Ti_{0.2}Zr_{0.2}Nb_{0.2}Hf_{0.2}Ta_{0.2})C$ in our work has similar lattice constants to TaC; this result is also illustrated in Figure 6b. Nearly 80% of the bond lengths are close to TaC in HEC, with an absolute error of less than 3%. Therefore, HEC has a lattice constant similar to that of TaC.

From the above analysis, we found that the reason why HEC has a lower thermal conductivity at room temperature is that it has a lower lattice thermal conductivity, induced by the terrible phonon scattering. Due to the diversity of metal atomic masses and radii, the cationic sublattices can have significant lattice distortion, and the anionic sublattice is distorted to balance this distortion. These severe lattice distortions result in phonon scattering. For transition metal carbides, the Fermi surface nesting, high electron density and perturbations in interatomic potentials induced by the large number of local atomic vibrations cause strong electron–phonon interactions and relatively weak phonon–phonon interactions [32,46,47], which appreciably suppress lattice thermal conductivity. Intuitively, a harmonic force constant plays a more important role in high-entropy carbides than binary carbides. This is because the multi-component configuration results in a more complex chemical environment for high-entropy carbides. Therefore, the HEC has a low thermal conductivity at room temperature.

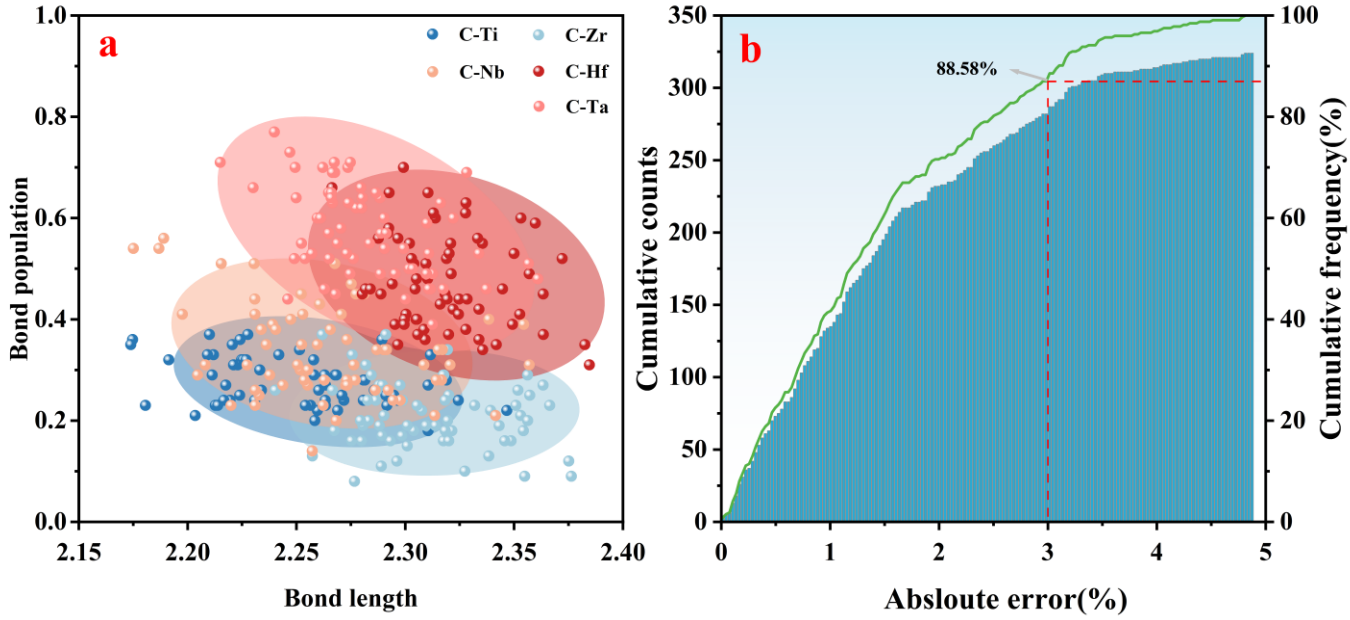

Figure 6. (**a**) The bond population (BP)–bond length (BL) of each bond (the dashed line represents the bond length in binary carbides); (**b**) the absolute error (%) between M-C in high-entropy carbide and TaC in binary carbide.

4. Conclusions

In summary, we have briefly described the changes in the electrical and thermal conductivity of $(Ti_{0.2}Zr_{0.2}Nb_{0.2}Hf_{0.2}Ta_{0.2})C$ (HEC) at room temperature. For the electrical conductivity, because the subtle differences in its electronic structure do not have a significant impact on it, we could use the ROM to evaluate and predict it. However, for the thermal conductivity, due to the serious lattice distortion in HEC, the scattering rate of the body was improved, and the complexity of the structure also inhibits the transport capacity of acoustic phonons for heat, so the thermal conductivity seriously deviates from the predicted value under the ROM.

Supplementary Materials: The following supporting information can be downloaded at: https://www.mdpi.com/article/10.3390/cryst13040708/s1, Figure S1: The phonon spectra of high-entropy carbides and individual carbides; Fig. S2. The Total-Density of states and Partial-Density of states of carbides and individual carbides.

Author Contributions: Conceptualization, T.L.; methodology, T.L. and J.Z.; software, T.L. and N.L.; validation, J.Z.; investigation, T.L.; formal analysis, T.L., N.L. and J.Z.; data curation, T.L., L.L., J.Z. and N.L.; writing−original draft preparation, T.L.; writing−review and editing J.Z., N.L. and L.L.; supervision J.Z. and N.L.; funding acquisition, N.L. and J.Z. All authors have read and agreed to the published version of the manuscript.

Funding: This research was funded by the National Natural Science Foundation of China (Grant Nos. 43200021), Wuhan University of Science and Technology (No. G201605).

Data Availability Statement: Not available.

Acknowledgments: The authors greatly acknowledge the financial support from the National Natural Science Foundation of China (Grant Nos. 43200021), the State Key Laboratory of Refractories and Metallurgy, Wuhan University of Science and Technology (No. G201605), and Fundamental Research Funds for the Central Universities (No. WUT35401053-2022).

Conflicts of Interest: The authors declare no conflict of interest.

References

1. Rost, C.M.; Sachet, E.; Borman, T.; Moballegh, A.; Dickey, E.C.; Hou, D.; Jones, J.L.; Curtarolo, S.; Maria, J.P. Entropy-stabilized oxides. *Nat. Commun.* **2015**, *6*, 8485. [CrossRef]
2. Talluri, B.; Yoo, K.; Kim, J. High entropy spinel metal oxide $(CoCrFeMnNi)_3O_4$ nanoparticles as novel efficient electrocatalyst for methanol oxidation and oxygen evolution reactions. *J. Environ. Chem. Eng.* **2022**, *10*, 106932. [CrossRef]
3. Gao, Y.; Liu, Y.; Yu, H.; Zou, D. High-entropy oxides for catalysis: Status and perspectives. *Appl. Catal. A Gen.* **2022**, *631*, 118478. [CrossRef]
4. Yu, P.; Ma, Z.; Liu, C.; Liu, W.; Zhao, S.; Han, Z.; Shao, T.; Gao, P.; Jiang, B.; Gu, X. Preparation of high entropy $(Ba_{0.2}Mg_{0.2}Ca_{0.2}Sr_{0.2}Pb_{0.2})TiO_3$ perovskite oxide powders by a sol-hydrothermal method. *Ceram. Int.* **2022**, *48*, 15992–15999. [CrossRef]
5. Rost, C.M.; Rak, Z.; Brenner, D.W.; Maria, J.P. Local structure of the $Mg_xNi_xCo_xCu_xZn_xO$(x = 0.2) entropy-stabilized oxide: An EXAFS study. *J. Am. Ceram. Soc.* **2017**, *100*, 2732–2738. [CrossRef]
6. Wang, C.; Qin, M.; Lei, T.; He, Y.; Kisslinger, K.; Rupert, T.J.; Luo, J.; Xin, H.L. Synergic grain boundary segregation and precipitation in W- and W-Mo-containing high-entropy borides. *J. Eur. Ceram. Soc.* **2021**, *41*, 5380–5387. [CrossRef]
7. Zhang, Y.; Jiang, Z.-B.; Sun, S.-K.; Guo, W.-M.; Chen, Q.-S.; Qiu, J.-X.; Plucknett, K.; Lin, H.-T. Microstructure and mechanical properties of high-entropy borides derived from boro/carbothermal reduction. *J. Eur. Ceram. Soc.* **2019**, *39*, 3920–3924. [CrossRef]
8. Barbarossa, S.; Orrù, R.; Garroni, S.; Licheri, R.; Cao, G. Ultra high temperature high-entropy borides: Effect of graphite addition on oxides removal and densification behaviour. *Ceram. Int.* **2021**, *47*, 6220–6231. [CrossRef]
9. Qin, Y.; Wang, J.-C.; Liu, J.-X.; Wei, X.-F.; Li, F.; Zhang, G.-J.; Jing, C.; Zhao, J.; Wu, H. High-entropy silicide ceramics developed from $(TiZrNbMoW)Si_2$ formulation doped with aluminum. *J. Eur. Ceram. Soc.* **2020**, *40*, 2752–2759. [CrossRef]
10. Kuang, J.; Zhang, P.; Wang, Q.; Hu, Z.; Liang, X.; Shen, B. Formation and oxidation behavior of refractory high-entropy silicide $(NbMoTaW)Si_2$ coating. *Corros. Sci.* **2022**, *198*, 110134. [CrossRef]
11. Liu, D.; Huang, Y.; Liu, L.; Zhang, L. A novel of MSi_2 high-entropy silicide: Be expected to improve mechanical properties of $MoSi_2$. *Mater. Lett.* **2020**, *268*, 127629. [CrossRef]
12. Kavak, S.; Bayrak, K.G.; Bellek, M.; Mertdinç, S.; Muhaffel, F.; Gökçe, H.; Ayas, E.; Derin, B.; Öveçoğlu, M.L.; Ağaoğulları, D. Synthesis and characterization of (HfMoTiWZr)C high entropy carbide ceramics. *Ceram. Int.* **2022**, *48*, 7695–7705. [CrossRef]
13. Zhang, P.-X.; Ye, L.; Chen, F.-H.; Han, W.-J.; Wu, Y.-H.; Zhao, T. Stability, mechanical, and thermodynamic behaviors of (TiZrHfTaM)C (M = Nb, Mo, W, V, Cr) high-entropy carbide ceramics. *J. Alloys Compd.* **2022**, *903*, 163868. [CrossRef]
14. Yan, X.; Constantin, L.; Lu, Y.; Silvain, J.F.; Nastasi, M.; Cui, B. $(Hf_{0.2}Zr_{0.2}Ta_{0.2}Nb_{0.2}Ti_{0.2})C$ high-entropy ceramics with low thermal conductivity. *J. Am. Ceram. Soc.* **2018**, *101*, 4486–4491. [CrossRef]
15. Dusza, J.; Švec, P.; Girman, V.; Sedlák, R.; Castle, E.G.; Csanádi, T.; Kovalčíková, A.; Reece, M.J. Microstructure of (Hf-Ta-Zr-Nb)C high-entropy carbide at micro and nano/atomic level. *J. Eur. Ceram. Soc.* **2018**, *38*, 4303–4307. [CrossRef]
16. Castle, E.; Csanadi, T.; Grasso, S.; Dusza, J.; Reece, M. Processing and Properties of High-Entropy Ultra-High Temperature Carbides. *Sci. Rep.* **2018**, *8*, 8609. [CrossRef]
17. Liu, D.; Zhang, A.; Jia, J.; Meng, J.; Su, B. Phase evolution and properties of (VNbTaMoW)C high entropy carbide prepared by reaction synthesis. *J. Eur. Ceram. Soc.* **2020**, *40*, 2746–2751. [CrossRef]
18. Lin, Y.-C.; Hsu, S.-Y.; Song, R.-W.; Lo, W.-L.; Lai, Y.-T.; Tsai, S.-Y.; Duh, J.-G. Improving the hardness of high entropy nitride $(Cr_{0.35}Al_{0.25}Nb_{0.12}Si_{0.08}V_{0.20})N$ coatings via tuning substrate temperature and bias for anti-wear applications. *Surf. Coat. Technol.* 2020; 403, 126417. [CrossRef]
19. Ye, B.; Wen, T.; Huang, K.; Wang, C.Z.; Chu, Y. First-principles study, fabrication, and characterization of $(Hf_{0.2}Zr_{0.2}Ta_{0.2}Nb_{0.2}Ti_{0.2})C$ high-entropy ceramic. *J. Am. Ceram. Soc.* **2019**, *102*, 4344–4352. [CrossRef]
20. Ye, B.; Wen, T.; Nguyen, M.C.; Hao, L.; Wang, C.-Z.; Chu, Y. First-principles study, fabrication and characterization of $(Zr_{0.25}Nb_{0.25}Ti_{0.25}V_{0.25})C$ high-entropy ceramics. *Acta Mater.* **2019**, *170*, 15–23. [CrossRef]
21. Liu, S.-Y.; Zhang, S.; Liu, S.; Li, D.-J.; Li, Y.; Wang, S. Phase stability, mechanical properties and melting points of high-entropy quaternary metal carbides from first-principles. *J. Eur. Ceram. Soc.* **2021**, *41*, 6267–6274. [CrossRef]
22. Lu, W.; Chen, L.; Zhang, W.; Su, W.; Wang, Y.; Fu, Y.; Zhou, Y. Single-phase formation and mechanical properties of (TiZrNbTaMo)C high-entropy ceramics: First-principles prediction and experimental study. *J. Eur. Ceram. Soc.* **2022**, *42*, 2021–2027. [CrossRef]
23. Schwind, E.C.; Reece, M.J.; Castle, E.; Fahrenholtz, W.G.; Hilmas, G.E. Thermal and electrical properties of a high entropy carbide (Ta, Hf, Nb, Zr) at elevated temperatures. *J. Am. Ceram. Soc.* **2022**, *105*, 4426–4434. [CrossRef]
24. Liu, D.; Hou, Y.; Meng, J.; Zhang, A.; Han, J.; Zhang, J. The significant influence of carbon content on mechanical and thermal properties of $(VNbTaMoW)_{0.5}C_x$ high entropy carbides. *J. Eur. Ceram. Soc.* **2022**, *42*, 5262–5272. [CrossRef]
25. Dai, F.-Z.; Wen, B.; Sun, Y.; Xiang, H.; Zhou, Y. Theoretical prediction on thermal and mechanical properties of high entropy $(Zr_{0.2}Hf_{0.2}Ti_{0.2}Nb_{0.2}Ta_{0.2})C$ by deep learning potential. *J. Mater. Sci. Technol.* **2020**, *43*, 168–174. [CrossRef]
26. Zhou, Q.; Zhang, J.; Fu, Z.; Wang, D. Microstructure and Mechanical Property of (TiNbTaZrHf)C Synthesized by In-situ Reaction. *J. Wuhan Univ. Technol.-Mater. Sci. Ed.* **2022**, *37*, 177–183. [CrossRef]
27. Clark, S.J.; Segall, M.D.; Pickard, C.J.; Hasnip, P.J.; Probert, M.I.J.; Refson, K.; Payne, M.C. First principles methods using CASTEP. *Z. Für Krist.-Cryst. Mater.* **2005**, *220*, 567–570. [CrossRef]
28. Segall, M.D.; Lindan, P.J.D.; Probert, M.J.; Pickard, C.J.; Hasnip, P.J.; Clark, S.J.; Payne, M.C. First-principles simulation: Ideas, illustrations and the CASTEP code. *J. Phys. Condens. Matter* **2002**, *14*, 2717–2744. [CrossRef]

29. Perdew, J.P.; Burke, K.; Ernzerhof, M. Generalized Gradient Approximation Made Simple. *Phys. Rev. Lett.* **1996**, *77*, 3865–3868. [CrossRef]
30. Yu, D.; Yin, J.; Zhang, B.; Liu, X.; Reece, M.J.; Liu, W.; Huang, Z. Pressureless sintering and properties of $(Hf_{0.2}Zr_{0.2}Ta_{0.2}Nb_{0.2}Ti_{0.2})C$ high-entropy ceramics: The effect of pyrolytic carbon. *J. Eur. Ceram. Soc.* **2021**, *41*, 3823–3831. [CrossRef]
31. Wang, F.; Yan, X.; Wang, T.; Wu, Y.; Shao, L.; Nastasi, M.; Lu, Y.; Cui, B. Irradiation damage in $(Zr_{0.25}Ta_{0.25}Nb_{0.25}Ti_{0.25})C$ high-entropy carbide ceramics. *Acta Mater.* **2020**, *195*, 739–749. [CrossRef]
32. Liang, X.; Wang, H.; Wang, C. Lattice thermal conductivity of transition metal carbides: Evidence of a strong electron-phonon interaction above room temperature. *Acta Mater.* **2021**, *216*, 117160. [CrossRef]
33. Liu, R.; Chen, H.; Zhao, K.; Qin, Y.; Jiang, B.; Zhang, T.; Sha, G.; Shi, X.; Uher, C.; Zhang, W.; et al. Entropy as a Gene-Like Performance Indicator Promoting Thermoelectric Materials. *Adv. Mater.* **2017**, *29*, 1702712. [CrossRef] [PubMed]
34. Rost, C.M.; Borman, T.; Hossain, M.D.; Lim, M.; Quiambao-Tomko, K.F.; Tomko, J.A.; Brenner, D.W.; Maria, J.-P.; Hopkins, P.E. Electron and phonon thermal conductivity in high entropy carbides with variable carbon content. *Acta Mater.* **2020**, *196*, 231–239. [CrossRef]
35. Makinson, R.E.B. The thermal conductivity of metals. *Math. Proc. Camb. Philos. Soc.* **2008**, *34*, 474–497. [CrossRef]
36. Kojda, D.; Mitdank, R.; Handwerg, M.; Mogilatenko, A.; Albrecht, M.; Wang, Z.; Ruhhammer, J.; Kroener, M.; Woias, P.; Fischer, S.F. Temperature-dependent thermoelectric properties of individual silver nanowires. *Phys. Rev. B* **2015**, *91*, 024302. [CrossRef]
37. Avery, A.D.; Mason, S.J.; Bassett, D.; Wesenberg, D.; Zink, B.L. Thermal and electrical conductivity of approximately 100-nm permalloy, Ni, Co, Al, and Cu films and examination of the Wiedemann-Franz Law. *Phys. Rev. B* **2015**, *92*, 214410. [CrossRef]
38. Körmann, F.; Ikeda, Y.; Grabowski, B.; Sluiter, M.H.F. Phonon broadening in high entropy alloys. *npj Comput. Mater.* **2017**, *3*, 36. [CrossRef]
39. Zhang, Z.; Zhu, S.; Liu, Y.; Liu, L.; Ma, Z. Phase structure, mechanical properties and thermal properties of high-entropy diboride $(Hf_{0.25}Zr_{0.25}Ta_{0.25}Sc_{0.25})B_2$. *J. Eur. Ceram. Soc.* **2022**, *42*, 5303–5313. [CrossRef]
40. Delaire, O.; Ma, J.; Marty, K.; May, A.F.; McGuire, M.A.; Du, M.H.; Singh, D.J.; Podlesnyak, A.; Ehlers, G.; Lumsden, M.D.; et al. Giant anharmonic phonon scattering in PbTe. *Nat. Mater.* **2011**, *10*, 614–619. [CrossRef]
41. Rubel, M.H.K.; Hossain, K.M.; Mitro, S.K.; Rahaman, M.M.; Hadi, M.A.; Islam, A.K.M.A. Comprehensive first-principles calculations on physical properties of ScV_2Ga_4 and ZrV_2Ga_4 in comparison with superconducting HfV_2Ga_4. *Mater. Today Commun.* **2020**, *24*, 100935. [CrossRef]
42. Xiong, K.; You, L.; Zhang, S.; Yang, L.; Jin, C.; Guo, L.; Wang, Y.; Mao, Y. Pressure and temperature effects on (TiZrTa)C medium-entropy carbide from first-principles. *J. Mater. Res. Technol.* **2023**, *23*, 2288–2300. [CrossRef]
43. Uporov, S.A.; Ryltsev, R.E.; Sidorov, V.A.; Estemirova, S.K.; Sterkhov, E.V.; Balyakin, I.A.; Chtchelkatchev, N.M. Pressure effects on electronic structure and electrical conductivity of TiZrHfNb high-entropy alloy. *Intermetallics* **2022**, *140*, 107394. [CrossRef]
44. Hong, D.; Zeng, W.; Liu, F.-S.; Tang, B.; Liu, Q.-J. The structural, mechanical and electronic properties of NbXSi (X = Fe, Co, Ni, Ru, Rh, Pd, Os, Ir and Pt) compounds from first-principles calculations. *Mater. Chem. Phys.* **2021**, *259*, 124029. [CrossRef]
45. Esters, M.; Oses, C.; Hicks, D.; Mehl, M.J.; Jahnatek, M.; Hossain, M.D.; Maria, J.P.; Brenner, D.W.; Toher, C.; Curtarolo, S. Settling the matter of the role of vibrations in the stability of high-entropy carbides. *Nat. Commun.* **2021**, *12*, 5747. [CrossRef] [PubMed]
46. Li, C.; Ravichandran, N.K.; Lindsay, L.; Broido, D. Fermi Surface Nesting and Phonon Frequency Gap Drive Anomalous Thermal Transport. *Phys. Rev. Lett.* **2018**, *121*, 175901. [CrossRef]
47. Yang, J.-Y.; Zhang, W.; Xu, C.; Liu, J.; Liu, L.; Hu, M. Strong electron-phonon coupling induced anomalous phonon transport in ultrahigh temperature ceramics ZrB_2 TiB_2. *Int. J. Heat. Mass. Transf.* **2020**, *152*, 119481. [CrossRef]

Disclaimer/Publisher's Note: The statements, opinions and data contained in all publications are solely those of the individual author(s) and contributor(s) and not of MDPI and/or the editor(s). MDPI and/or the editor(s) disclaim responsibility for any injury to people or property resulting from any ideas, methods, instructions or products referred to in the content.